Aerospace Science and Technology 178 (2026) 113231

Contents lists available at ScienceDirect

Aerospace Science and Technology

journal homepage: www.elsevier.com/locate/aescte

Effects of distributed propulsion on commuter aircraft longitudinal static stability and control

Danilo Ciliberti *, Fabrizio Nicolosi

Department of Industrial Engineering, University of Naples Federico II, Via Claudio 21, Naples, 80125, Italy

ARTICLE INFO

Communicated by Kontis Konstantinos

Keywords:
Distributed propulsion
Wind tunnel testing
Experimental aerodynamics
Aircraft stability and control

ABSTRACT

This paper presents wind-tunnel results quantifying the impact of a leading-edge distributed high-lift propeller system on the longitudinal stability and control characteristics of a generic 19-seat commuter aircraft model. The experimental campaign extends previous power-off tests on the same configuration to powered conditions, measuring lift, drag, and pitching-moment coefficients versus angle of attack and thrust coefficient at take-off flap setting. Results show that distributed propulsion affects longitudinal stability and control depending on thrust level and tail configuration—conventional aft-tail or T-tail—highlighting effects that are overlooked in literature. Static margin can be reduced by 8% or increased up to 6%, whereas the elevator control power can be doubled. Implications for tail sizing, pitch trim, and take-off performance are discussed.

1. Introduction

In the last 15 years, there has been a growing interest in (hybrid-) electric aeronautical architectures coupled with distributed electric propulsion (DEP), which emerged as a promising way to exploit aero-propulsive interactions [1–3]. In DEP layouts, thrust is generated by an array of propulsors smaller than a single conventional propeller of equivalent total thrust, distributed along one or more lifting surfaces, enabling higher effective dynamic pressure and thus enhancing low-speed performance [4–6]. Several studies and roadmaps have highlighted the potential of DEP to reduce energy consumption and emissions of regional and small-air-transport aircraft, particularly for missions below approximately 300 nautical miles where battery specific energy is compatible with meaningful payloads [7–10].

The aforementioned studies established that the impact of DEP on aircraft design strongly depends on the aero-propulsive effects that can be achieved. Consequently, many authors focused on the understanding of the physical interaction of a distributed propulsion system with a lifting surface—through propeller blowing or boundary layer ingestion—and on the prediction of the enhanced aerodynamics [5,6,11–20]. Another research topic is on the application of these effects in aircraft preliminary design, evaluating the impact on aircraft mass, performance, and pollutants emission [9,21–26].

However, as is common in the DEP literature, much of the emphasis has been placed on lift augmentation, drag penalties, and overall aerodynamic efficiency, with comparatively fewer quantitative results on *pitching-moment behavior, static-margin shifts, and elevator control power* under DEP operation.

Most of the investigations have been performed with numerical methods. For instance, studies like [11,23,27–29] are based on high-fidelity RANS CFD, typically modeling propellers as actuator disks, focusing primarily on lift and drag increments as functions of propeller position, thrust coefficient, and flap setting. Besides the wing-propeller coupling, the effects of aerodynamic interactions between adjacent propellers have been experimentally investigated by de Vries et al. [30], who tested a wing which spanned the entire test section width (no wingtip vortices), estimating changes in lift, drag, and noise with respect to the standalone propeller case. However, no considerations on aircraft stability and control were made in these studies.

A first systematic investigation that included the pitching moment was made by the authors [6], who exploited high-fidelity numerical analyses to assess the mutual effects between wing and propeller on a rectangular planform with different flap deflections. Results highlighted that lift increment is always accompanied by drag increase and additional pitch-down moment, while the propulsive efficiency of the propeller may also be affected. Refs. [31,32] also acknowledged the importance of pitching moment estimation with blown high-lift systems, yet the impact on aircraft design and performance was not estimated. At aircraft level, Refs. [18,25,26] exploited high-fidelity RANS CFD analyses to assess the potential of DEP on a regional turboprop in cruise and landing conditions, relating the thrust distribution to the aerodynamic efficiency, without assessing the impact on aircraft stability and

* Corresponding author.
E-mail address: danilo.ciliberti@unina.it (D. Ciliberti).

https://doi.org/10.1016/j.ast.2026.113231
Received 19 May 2026; Received in revised form 10 July 2026; Accepted 15 July 2026
Available online 17 July 2026
1270-9638/

control. Similarly, Chen et al. [33], in a recent wing optimization study under distributed slipstream, confirmed that existing DEP research overwhelmingly focuses on lift and drag increments, while the impact on pitching moment remains largely unexplored.

Thus, while DEP literature has a strong wing-scale component, only some works addressed aircraft-scale static stability and control, and only for specific demonstrators, not for an aircraft class. Nguyen Van et al. [22] investigated the impact of DEP on aircraft directional control, claiming a potential 60% reduction in vertical tail area with differential thrust control. Similarly, Hoogreef and Soikkeli [34] investigated a modified X-57 aircraft, finding that distributed propulsion has the potential to replace the rudder during the engine inoperative condition in climb. Kim et al. [35] analyzed the aerodynamic and static-stability characteristics of a manned distributed-propulsion personal aerial vehicle and a quad-tilt-propeller UAV using actuator-based methods. Their results showed that aero-propulsive coupling can significantly reduce static stability—to the point of rendering the UAV configuration statically unstable—while the larger manned configuration remains stable owing to different geometry and mass distribution. Cacciola et al. [36] derived stability and control derivatives as functions of advance ratio of their UAV demonstrator from VLM-based models and flight-test data. Schollenberger et al. [37] provided flight simulation results correlated with flight test data of an unmanned scaled demonstrator with DEP, where the aircraft was certainly required to be trimmed in cruise, but no analysis of its stability and control characteristics was provided.

Qin et al. [38] investigated the aero-propulsive coupling dynamics of a DEP tandem-wing UAV designed for rapid ascent. By incorporating distributed propeller slipstream effects into a framework based on classical stability derivatives, they analyzed how DEP modifies the natural modes of motion—in particular showing that the phugoid eigenvalues degrade into two overdamped real roots with increasing thrust, while the short-period mode is accelerated by the large rear-wing damping. Ground-based blown-wing experiments and actual flight tests validated the model. Although this work provides valuable insight into dynamic stability, the platform is a small UAV in rapid-ascent conditions and does not address the static stability and elevator control authority of a conventional aft-tail layout in take-off configuration.

The dependence of pitching moment on thrust level has been further quantified analytically by Wei et al. [39], who constructed an explicit polynomial model of the longitudinal aerodynamic coefficients as functions of angle of attack, flap deflection, and the momentum-excess coefficient for the NASA X-57 distributed propulsion system. Their results showed that for sufficiently large momentum-excess coefficients, the pitching-moment slope with respect to angle of attack becomes positive beyond a certain angle of attack, indicating a transition to static longitudinal instability—a finding that directly motivates the experimental quantification of static margin shifts pursued in the present work.

The literature reviewed above supports several conclusions. First, DEP and related blown-wing concepts have been extensively studied in terms of lift and drag increments, at both wing and aircraft level, and there is a growing body of works integrating aero-propulsive effects into conceptual design and sizing frameworks. Second, multiple studies have shown that DEP lift augmentation is typically accompanied by increased pitching-down moment coefficients, implying potential penalties in static margin and trim. Third, while a few works have begun to quantify how DEP affects aircraft-level stability and control derivatives, they focus on UAVs, eVTOLs, or specific demonstrators, relying on numerical models and system identification rather than extensive wind-tunnel measurements for a specific aircraft class.

What is still absent from the open literature is a comprehensive, experimentally based characterization of how a leading-edge high-lift propeller system installed on a commuter-class blown wing modifies:

- the full set of longitudinal aerodynamic coefficients (lift C_L, drag C_D, and pitching moment C_M) as functions of angle of attack and thrust coefficient at one or more flap settings;
- the longitudinal static stability derivative, the position of the neutral point, and thus the static margin $\mathrm{d}C_M/\mathrm{d}C_L$ for different horizontal-tail layouts (conventional aft tail vs. T-tail);
- the elevator control derivative $\mathrm{d}C_M/\mathrm{d}\delta_e$ and available control power as a function of DEP thrust level.

The present work addresses the literature gaps outlined above with a generic commuter aircraft model, previously characterized in power-off tests [40], extending the experimental campaign to powered conditions with distributed propellers. By extracting and correlating the relevant aerodynamic derivatives from wind tunnel data with thrust coefficient, angle of attack, and elevator deflection angle, the study provides design-relevant insight into how DEP affects tail sizing, pitch trim, static margin, and elevator control authority for the commuter aircraft class in take-off configuration. This characterization and the subsequent modeling of incremental effects constitute the novel contributions filling the identified gap on the impact of distributed propulsion on the longitudinal stability and control of a fixed-wing aircraft.

The generic 19-passenger commuter aircraft with DEP has been developed as a subscale technology demonstrator for the Italian PROSIB project. The platform features a high wing with slotted flaps, alternative empennage layouts (conventional aft tail and T-tail), and provision for a belly-mounted pod housing batteries and hybrid-electric systems.

The remainder of the text is structured as follows. Section 2 describes the experimental setup including the wind tunnel facility, the aircraft model and the installation of the DEP system, similarity parameters, test matrix, and data reduction. Section 3 provides the results of wind tunnel runs, presenting the variations of the aerodynamic coefficients, as well as the derived quantities for the evaluation of longitudinal stability and control characteristics, for selected configurations (wing-body, alternative tails) at different thrust settings. A discussion on design and operational implications follows, including the impact of tailplane layout, static margin, and trim penalty; control power margins at different thrust levels and attitudes; interaction with performance benefits and losses. Concluding remarks are drawn in Section 4.

2. Wind tunnel setup

The experimental tests were run in the Department's closed-return, closed-test section, subsonic wind tunnel. The test section has a tempered rectangular shape 2.0 m wide and 1.4 m high. The average turbulence intensity at test section inlet is 0.10%.

The hardware to measure the aero-propulsive forces on the model were: an ATI Delta SI-165-15, a six degrees of freedom internal strain gauge balance to measure the aerodynamic forces and moments on the aircraft model; four off-center unidirectional load cells to measure the thrust produced by the propellers; electronic sensor to measure motors' voltage, current, and RPM.

The data acquisition and control system was made up of the following devices: a National Instruments USB-6341 board to acquire wind tunnel aerodynamic data and balance readings; a National Instruments USB-6343 board to acquire motor data, propulsive forces, and to control the motors' rotational rate; desktop computers to run LabVIEW virtual instruments reading the data acquisition and control devices, one for the wind tunnel and another for the propulsive group. Details on the aircraft model and thrust measurements are given in the following.

2.1. Scaled aircraft model

The experimental model is representative of a generic 19-pax airplane [40]. Detailed dimensions are reported in Figs. 1 and 2. The model had a planform area of 0.25 m^2, a mean aerodynamic chord of 0.171 m, a wing span of 1.5 m, an overall length of about 1.1 m. The airfoils were the NACA 23018 for the wing root and kink sections, the NACA 23015 for the wing tip section, and the NACA 0012 for the tailplane sections. The test article was entirely made in aluminum alloy by CNC manufacturing. The tailplanes group could be entirely removed from the fuselage

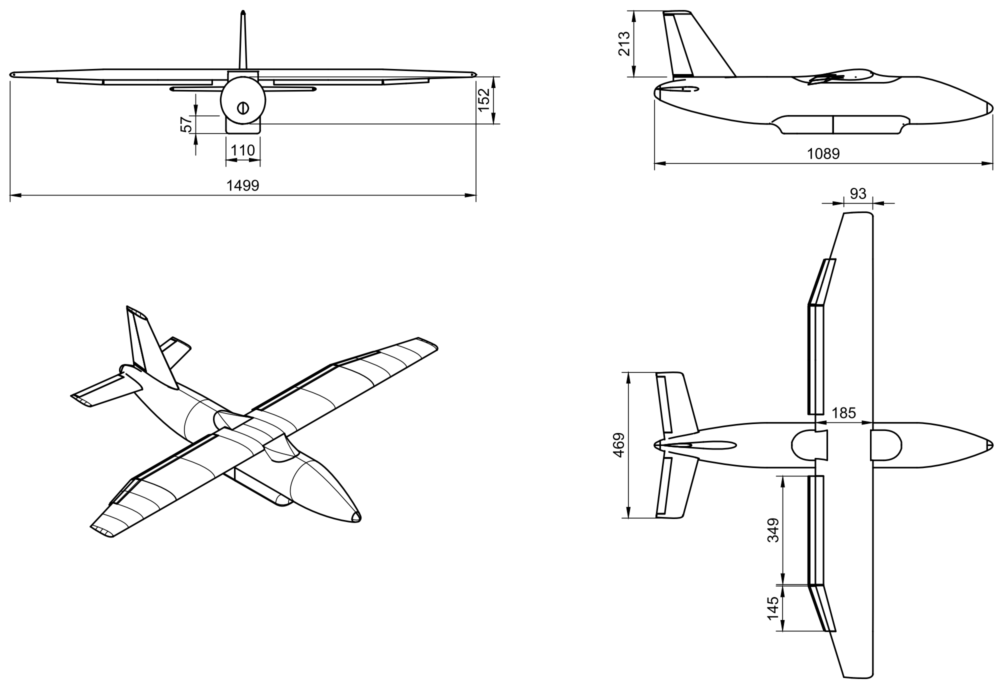

Fig. 1. Aircraft model drawings. Units in mm.

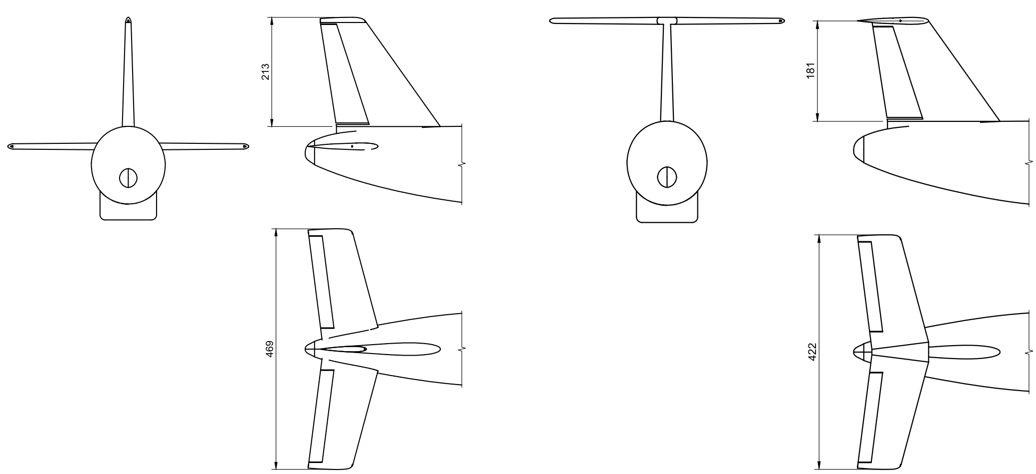

(a) Conventional tail. (b) T-tail.

Fig. 2. The alternative tail configurations. Units in mm.

to be quickly swapped. Fig. 3 shows the aircraft model in the test section with the two tailplanes (conventional aft and T-tail). In this work, a DEP frame with 10 propellers has been added in the wind tunnel test section. Details are given in the following sections.

2.2. Scaling effects

Thrust similarity requires that the nondimensional thrust coefficient of the scaled model is the same of the full-scale aircraft. An ideal propeller scaling would also require the same torque coefficient but, since thrust and power scales differently, it is only possible to match one parameter [41]. For this research work, it was decided to match the thrust coefficient defined as:

$$T_c = \frac{T/n}{A_p q_\infty} \tag{1}$$

where T is the total thrust, n is the number of propellers, A_p is the disk area of a single propeller, q_∞ is the dynamic pressure. This definition is directly related to the airspeed in the assigned conditions and it is independent from the propeller's RPM. Note that T_c as defined here represents the thrust coefficient per propeller, with T/n being the thrust per propeller.

Take-off conditions were assigned. Therefore, assuming values for the aircraft maximum weight, thrust-to-weight ratio, lift coefficient, airspeed, the number of propellers, and their size, an estimation of T_c was made. The assumed values are reported in Table 1. With these data, a T_c ranging from 0.9 to 1.5 was estimated from Eq. (1) for an array of 10 distributed propellers. With a geometrical scale factor of 1:12 and a wind tunnel speed of 17 m/s, this converts to a single scaled propeller thrust from 20 N to 30 N. The propeller-motor coupling had to achieve this thrust range to simulate the take-off run conditions in the wind tunnel.

The combination of model's size and tunnel speed yielded a Reynolds number $Re \approx 2 \times 10^5$. Transition strips were applied to all lifting surfaces prior to testing, enforcing turbulent boundary layer conditions and eliminating laminar separation bubbles that typically inflate drag coef-

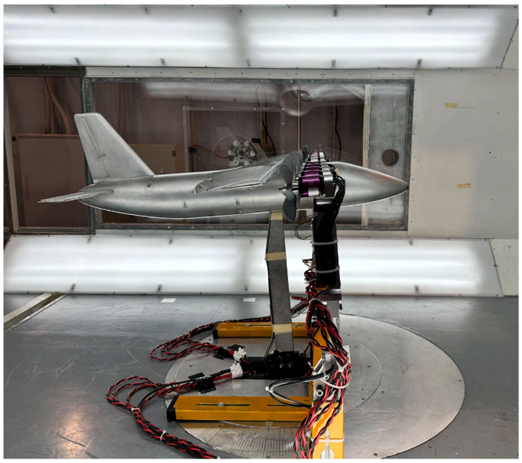

(a) Conventional aft tail

(b) T-tail

Fig. 3. The aircraft model in the wind tunnel with the two tailplane layouts.

Table 1
Assumed parameters to estimate thrust coefficient during the take-off run for a commuter aircraft with distributed propulsion. Data for the full-scale aircraft.

Parameter	Symbol	Value	Unit
Thrust-to-weight ratio	T/W	0.25 to 0.40	-
Take-off weight[a]	W	83,400	N
Total thrust	T	20,850 to 33,350	N
Single propeller area	A_p	1.64	m^2
Maximum lift coefficient	$C_{L,max}$	2.3	-
Stall speed	V_{min}	39.4	m/s
Take-off speed (20% margin)	V_∞	47.2	m/s
Dynamic pressure	q_∞	1367	Pa

[a] Below CS-23 limit for commuter aircraft (19000 lb).

ficients at low Reynolds numbers. Furthermore, the high-RPM propeller slipstream provided additional turbulent forcing over the blown wing region, ensuring that the boundary layer state on the model was representative of full-scale conditions.

2.3. Distributed thrust measurement

The distributed electric propulsion system installed in the wind-tunnel test section comprised ten brushless motors (Hacker A30-12 XL V4 Kv 700) with identical composite propellers [42] of about 0.12 m diameter, mounted on a dedicated support structure ahead of the wing. Thrust was measured using four calibrated load cells integrated into the propulsion support structure, as shown in Fig. 4. The support frame was constrained on the test section floor and had to be manually tilted to match the aircraft attitude, so that the geometric angle of attack was fixed during a wind tunnel run.

The frame was designed to keep the propulsive line close to the wing leading edge, yet detached from the aircraft model. To this end, the present work isolates the indirect aerodynamic effects of distributed propeller blowing on the airframe. Direct propulsive contributions, including thrust-line and propeller normal-force moments, were intentionally excluded from the aircraft balance measurements; accordingly, only net thrust was measured to define the thrust coefficient T_c. The frame was also designed to avoid any obstruction between the propellers and the wing. For this reason, the propellers were mounted downstream of the motors, while minimizing the frontal area of the propulsive line to limit the aerodynamic interference of the support frame. See also the side view in Fig. 5 illustrating the arrangement of propeller, motor, and electronic speed controller (ESC).

Table 2
Test matrix nomenclature: WB is wing-body configuration; WBHV is wing-body-horizontal-vertical configuration.

Config.	δ_e (deg)	Notes
WB	n.a.	fixed wing-propeller position, α and T_c sweep
WB	n.a.	effects of wing-propeller relative position, fixed α
WBHV	0°	complete aircraft with conv. aft tail, α and T_c sweep
WBHV	−10°	complete aircraft with conv. aft tail, α and T_c sweep
WBHV	0°	complete aircraft with T-tail layout, α and T_c sweep
WBHV	−10°	complete aircraft with T-tail layout, α and T_c sweep

A pre-test calibration with stationary propellers identified the aerodynamic drag contribution of the support structure as a function of dynamic pressure q_∞ and support attitude for each load cell. During powered tests, this drag contribution D_{cell} was subtracted from the raw load cell readings F_{cell} to obtain the net propeller thrust:

$$T_{\mathrm{net}} = \sum_{i=1}^{4} \left(F_{\mathrm{cell},i} - D_{\mathrm{cell},i} \right) \tag{2}$$

The propulsive data acquisition and motors' control were made in a dedicated LabVIEW virtual instrument. The additional solid blockage due to the DEP support frame was accounted for in the wind-tunnel correction software.

Because the RPM of individual propellers occasionally differed despite a common commanded throttle setting, thrust equalization across the propulsive line was ensured by monitoring the four load-cell (balance) readings rather than by matching per-propeller rotational speed. RPM was recorded primarily as a consistency check, with further details on its measurement and uncertainty given in Section 2.5.

2.4. Test matrix

The wind tunnel test matrix is given in Table 2. All runs were made at three different geometric angles of attack ($\alpha_g = 0°, 5°, 8°$) and at a fixed flap deflection angle ($\delta_f = 15°$). All powered runs were made with T_c from 0 to 1.66. The elevator deflection was set at $\delta_e = 0°, -10°$ for the complete aircraft configurations.

2.5. Measurement uncertainty

Net thrust was obtained from four HBM PW6C single-point load cells (10 kg capacity, accuracy class C3MR, multi-range). According to the manufacturer's specifications, the combined non-linearity, hysteresis, and off-center load error is on the order of ±0.02% of rated output,

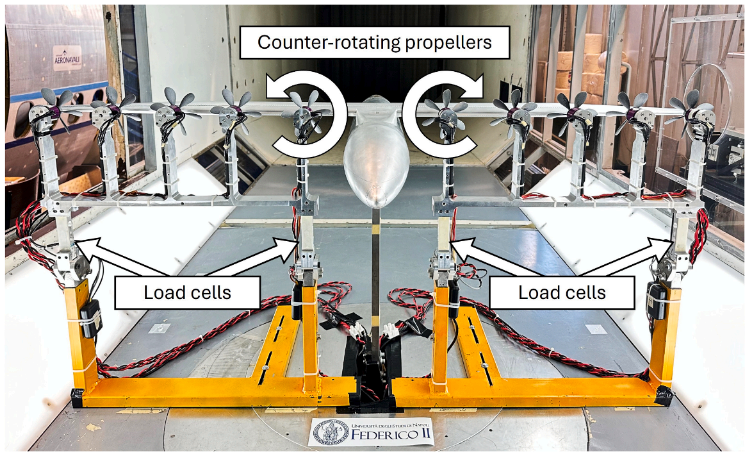

Fig. 4. Front view of the distributed propellers supporting frame in the wind tunnel test section.

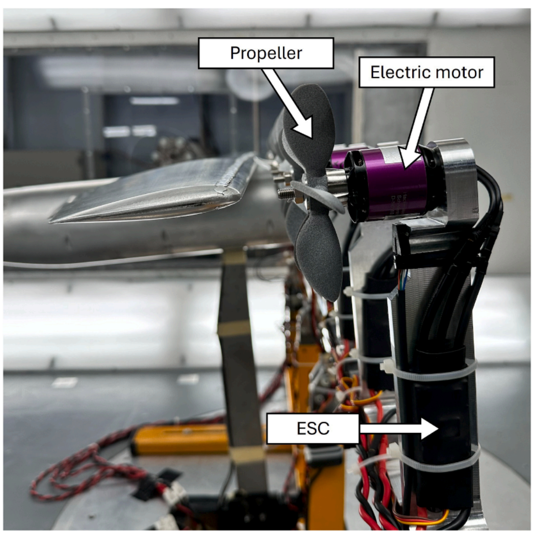

Fig. 5. Arrangement of the propulsive line with respect to the wing leading edge.

corresponding to an absolute uncertainty of about ±0.02 N per cell at full scale. Given the four-cell summation used to compute net thrust (2), and accounting for the pre-test drag-tare subtraction described in Section 2.3, the propagated uncertainty on T_{net} is estimated at approximately ±0.1 N, consistent with the resolution needed to distinguish the tested thrust levels (20–30 N per propeller). As noted in Section 2.3, individual propeller thrust could not be reliably inferred from RPM alone, since rotational speed occasionally differed measurably across the ten propellers. The load-cell readings, rather than per-propeller RPM, were therefore used to ensure an even thrust distribution during testing.

Motor RPM was measured using an OPB704WZ reflective infrared object sensor (890 nm LED/phototransistor pair) detecting a reflective marker on the outrunner motor rotor once per revolution. The sensor's pulse train was converted into an analog voltage proportional to RPM by a custom-made signal-conditioning board, outsourced to a third-party electronics manufacturer, built around an LM2917 frequency-to-voltage converter with INA128 instrumentation amplifiers for signal buffering and scaling prior to acquisition. Because the optical sensor itself functions purely as a digital on/off trigger, the accuracy of the RPM measurement chain is governed by the calibration of this conditioning board rather than by the sensor's own specifications.

Random errors on the aerodynamic coefficients were estimated from repeated tests at different angles of attack and thrust settings, with an average uncertainty of ±0.01 for C_L, ±0.0025 for C_D, and ±0.025 for C_M. These uncertainties, combined with the thrust-measurement error described above, propagate into the longitudinal stability and control derivatives presented in Section 3.3, which are evaluated via linear regression of the pitching moment coefficient vs. the angle of attack or the elevator deflection angle at different thrust levels. The corresponding regression-based confidence intervals are reported alongside the relevant results.

3. Results and discussion

Wind tunnel results were corrected for blockage and other effects according to [41,43]. The combined propellers size was about 4% of the wind tunnel cross-section area. Therefore, the airspeed correction due to propellers operating at full thrust was negligible [41]. The aerodynamic coefficients C_L (lift), C_D (drag), and C_M (pitching moment) were evaluated from the corrected balance readings. The moment reference point was fixed at 25% of the mean aerodynamic chord.

A first set of wind tunnel runs was made on the wing-body (WB) configuration to investigate the aero-propulsive effects on the main lifting surface. Then, having established the trends of the WB aerodynamic coefficients with angle of attack and thrust settings, the influence of wing-propeller relative position was investigated. Finally, the complete aircraft configuration with the two different tailplane layouts was tested to highlight the aero-propulsive effects on the longitudinal static stability and control characteristics of the aircraft model. Details are given in the following sections, where the charts' legend use the following nomenclature:

Prop-off, no frame indicates that the propulsive frame was folded to the floor without propellers (practically identical to the conditions of [40]);

Prop-off, with frame indicates that the propulsive frame was set up as in powered tests, but without propellers;

$\mathbf{T_c = 0}$ indicates that the tests were prop-on, with propellers rotating but providing zero net thrust (idle condition);

$\mathbf{T_c > 0}$ indicates that the tests were prop-on, with propeller providing positive thrust.

3.1. Effects of DEP on wing aerodynamics

Wind tunnel results for the wing-body configuration provided insights on how DEP affects the wing aerodynamics at 15° flap settings.

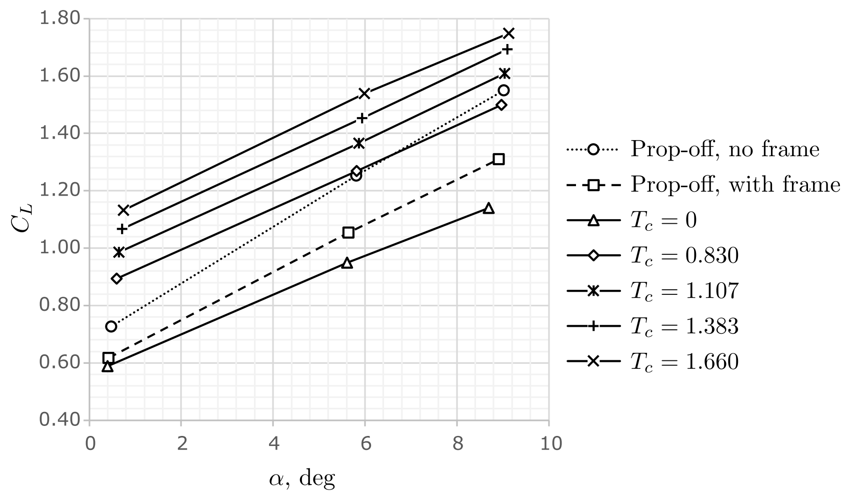

Fig. 6. Lift coefficient vs. angle of attack for the WB configuration.

Fig. 6 illustrates the variations of lift coefficient C_L with angle of attack α and thrust setting T_c. The dotted and dashed lines represent the WB configuration without propellers, with the former representing the case with the propulsive frame folded on the floor. The detrimental effect of the propulsive frame is apparent. Its presence reduced the lift curve slope $\mathrm{d}C_L/\mathrm{d}\alpha$ by about 15% and the value of the lift coefficient at zero angle of attack C_{L_0} by about 0.1. The installation of the propellers and their operation in idling condition ($T_c = 0$) caused a further 18% reduction of $\mathrm{d}C_L/\mathrm{d}\alpha$ and 0.03 decrement of C_{L_0}. Conversely, positive thrust settings increased $\mathrm{d}C_L/\mathrm{d}\alpha$ from 8% to 10% with respect to idling conditions, while C_{L_0} increased by about 0.10 per 0.28 increment of T_c.

The reader may note that the markers of Fig. 6 are not exactly located at fixed values of the angle of attack, with these values slightly moving to the right with increasing thrust settings. This is due to the correction of the flow curvature with lift coefficient. Generally, as the lift force generated by a wing increases, so does the downward acceleration of the flow. However, in a closed test section the downwash is partially obstructed by the floor. Therefore, the corrected values of the angles of attack reported in the charts are slightly larger than their geometrical values, which were exactly fixed at $0°, 5°, 8°$.

The drag polar shown in Fig. 7 illustrates the increase in drag coefficient due to the frame (about 100 drag counts at $C_L = 1$) and idling propellers (additional 250 drag counts at $T_c = 0$). Positive thrust settings were beneficial with respect to idling conditions, although the largest aerodynamic efficiency, evaluated as the ratio between lift and drag coefficients, was obtained with the prop-off configurations. This lift-to-drag ratio is plotted against the lift coefficient in Fig. 8. The reduction of aerodynamic efficiency with respect to the prop-off configurations is apparent. In average, from 2 to 4 points were lost due to the propulsive frame interference. A partial, but insufficient recovery was measured with the propellers blowing.

As expected, the additional lift due to DEP also affected the configuration's pitch tendency. Fig. 9 shows the pitching moment coefficient C_M vs. the angle of attack α. The aerodynamic interference of the propulsive frame reduced the magnitude of the C_M by about 0.010 at low angles of attack and sensibly more at larger angles. In other words, as C_L decreased due to the aerodynamic interference of the propulsive frame and idling propellers, so did the C_M. Moreover, the slope of the curve $\mathrm{d}C_M/\mathrm{d}\alpha$ at $T_c = 0$ was increased by about 20% with respect to the prop-off configuration with the propulsive frame folded, indicating that the destabilizing contribution of the wing-body was further aggravated under idling conditions. However, the application of positive thrust restored the initial value of $\mathrm{d}C_M/\mathrm{d}\alpha$ for low values of the angle of attack.

The shift of the wing-body aerodynamic center, evaluated as:

$$\Delta\bar{x}_{\mathrm{ac}} = -\frac{\mathrm{d}C_M/\mathrm{d}\alpha}{\mathrm{d}C_L/\mathrm{d}\alpha} \tag{3}$$

was estimated to be between 3% and 7% ahead of the reference position, which was at 25% of the mean aerodynamic chord, increasing with the thrust coefficient except for $T_c = 0$, where it achieved the maximum value.

Finally, a significant increase of the absolute value of C_M with T_c was observed. At low angles of attack, it nearly doubled in magnitude, from approximately −0.1 to −0.2, highlighting possible issues in longitudinal trim, if the elevator control power of the complete aircraft configuration were unaffected. Details on longitudinal stability and control under DEP operations are given in Section 3.3.

3.2. *Effects of propellers position on the wing aerodynamics*

During the investigation of the wing-body combination, the thrust lines of the DEP system were aligned to the wing chord. However, it was questioned whether the wing-propeller relative position could have an impact on the aerodynamics, as shown in [6]. Therefore, a total of seven positions were investigated, as illustrated in Fig. 10. To limit the number of the tests, two thrust settings and one value of the geometric angle of attack were selected. The results discussed in the previous section referred to the position labeled as A. By moving the propulsive frame on the illustrated points, a noticeable impact was obtained on the aerodynamic coefficients.

Wind tunnel runs were performed at $T_c = 1.383$ and $T_c = 1.660$ at $\alpha_g = 5°$, corresponding to a corrected angle of attack $\alpha \approx 6°$. Fig. 11 reports the variations of the aerodynamic coefficients with respect to $T_c = 0$. It is apparent the significant impact of propellers' position on the drag coefficient, with a reduction of about 55% at position F. Conversely, the lift and pitching moment coefficients were affected much less. As a consequence, the aerodynamic efficiency was largely improved, with position F ranked as the best, B as a potential competitor, and C as the worst. The increment in lift-to-drag ratio at F was almost independent from thrust settings, as C_L/C_D increased by about 1 with respect to the reference case $T_c = 0$ and by about 2.5 with respect to position A. The higher efficiency was attributed to a more favorable circulation that delayed flow separation, while lift and pitching-moment characteristics were only weakly affected.

3.3. *Effects of DEP on longitudinal stability and control*

The complete aircraft configurations (WBHV) were investigated with two tailplane groups: a conventional aft tail and a T-tail, already shown

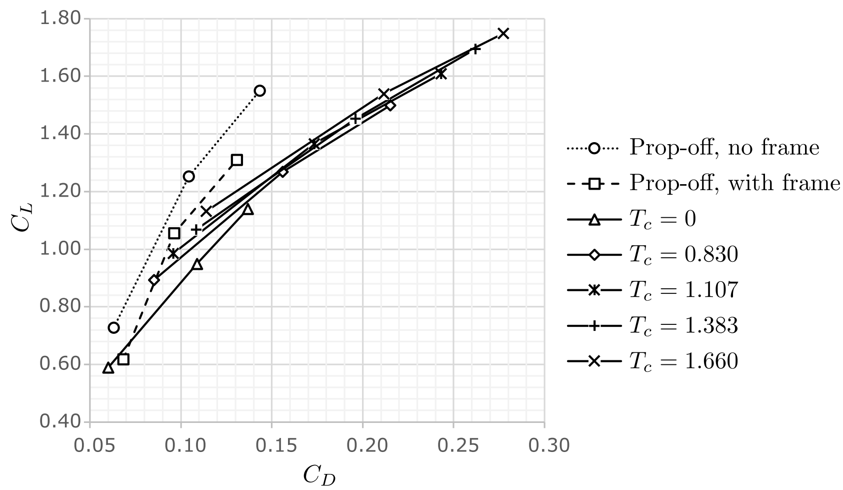

Fig. 7. Drag polar of the WB configuration.

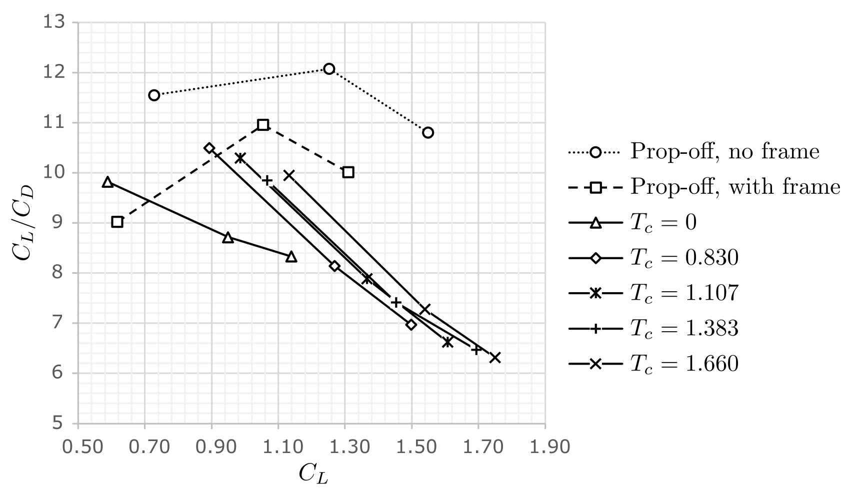

Fig. 8. Lift-to-drag ratio vs. lift coefficient for the WB configuration.

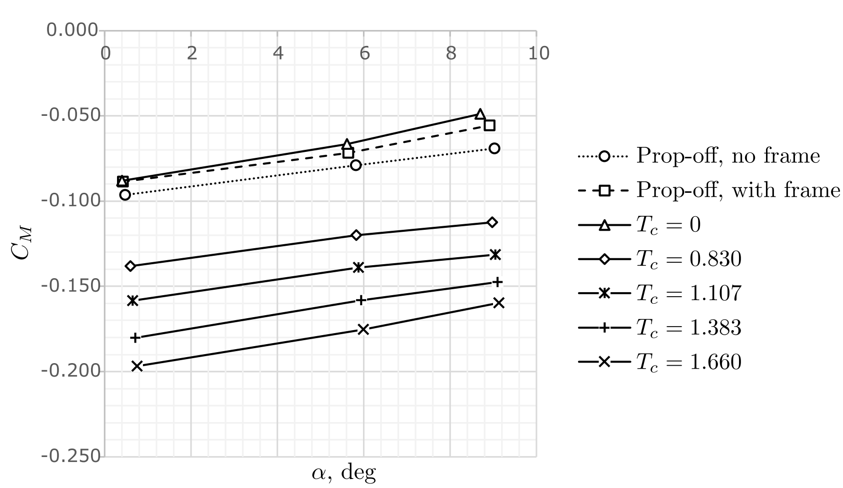

Fig. 9. Pitching moment coefficient vs. angle of attack for the WB configuration.

in Fig. 3. The propulsive line was set in position F, since it was the most favorable layout for the wing aerodynamic efficiency. Wind tunnel runs with the elevator fixed at $\delta_e = 0°$ and $-10°$ provided untrimmed results, because the rotational equilibrium ($C_M = 0$) was not always achieved.

The effects of DEP on lift and drag coefficients are shown in Figs. 12 and 13, respectively. The trends were similar to those observed in Section 3.1. An increase in lift curve slope with respect to the wing-body configuration was expected due to the additional rear lifting surface in untrimmed condition. The conventional aft tail and the T-tail layouts exhibited no appreciable differences in lift and drag characteristics.

Conversely, the pitching moment of the two tailplane configurations, shown in Fig. 14, provided different outcomes. The addition of

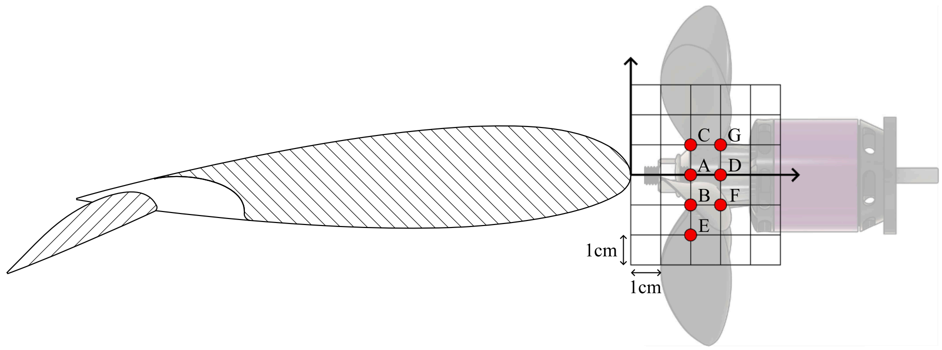

Fig. 10. Illustration of the relative wing-propeller positions. In this picture, the propulsor is located in A. Other positions are obtained by translating the entire propulsive assembly by the values indicated on the grid.

Table 3
Longitudinal stability derivatives at different thrust settings. Values in $\deg^{-1}$.

	Conventional tail			T-tail		
T_c	$dC_L/d\alpha$	$dC_M/d\alpha$	dC_M/dC_L	$dC_L/d\alpha$	$dC_M/d\alpha$	dC_M/dC_L
prop-off	0.104	−0.0222	−0.213	0.103	−0.0225	−0.220
0	0.079	−0.0169	−0.211	0.080	−0.0240	−0.298
0.830	0.089	−0.0238	−0.267	0.089	−0.0228	−0.258
1.107	0.096	−0.0254	−0.266	0.092	−0.0225	−0.245
1.383	0.098	−0.0259	−0.265	0.096	−0.0214	−0.224
1.660	0.100	−0.0268	−0.267	0.107	−0.0214	−0.220

the horizontal tail introduced the longitudinal stability at all conditions, since $dC_M/d\alpha < 0$. Both tailplanes exhibited the same value of $-0.022\,\deg^{-1}$ in prop-off condition. From there, positive thrust settings increased the $dC_M/d\alpha$ up to $-0.027\,\deg^{-1}$ on the conventional tail layout. This was attributed to the blowing effect of the propellers impinging on the tailplane, reducing the downwash gradient and increasing the local dynamic pressure. Conversely, the T-tail contribution to the pitch-down tendency was slightly reduced to $-0.021\,\deg^{-1}$ at full power, as the horizontal stabilizer was largely outside the propellers wake. Although it was not possible to measure dynamic and unsteady derivatives, it is expected that the changes in $dC_M/d\alpha$ would increase the pitch stiffness for the conventional tail and reduce it for the T-tail configuration, hence affecting the short-period response of the aircraft.

The other apparent effect of DEP visible in Fig. 14 is the downward translation of the C_M curves with increasing T_c values. At positive angles of attack and maximum thrust the C_M of the conventional tail changed by about -0.175 from idling conditions. Since the T-tail was outside the propeller wake, it caused a shift of about -0.125 in the same conditions. Full throttle settings provided a difference of about 0.045 between the two tailplane configurations. These negative increments of C_M must be compensated by the elevator to trim the aircraft (i.e. ensure $C_M = 0$) during DEP operation.

Because distributed propulsion simultaneously augments lift and pitch-down moment, comparing $dC_M/d\alpha$ across thrust settings is potentially misleading: at the same angle of attack, different thrust coefficients produce different lift coefficients, so the operating conditions are not aerodynamically equivalent. The derivative dC_M/dC_L, equivalent to the ratio between $dC_M/d\alpha$ and $dC_L/d\alpha$, provides a thrust-consistent reference by mapping the pitching moment against the actual aerodynamic loading state, and is a direct measure of the aircraft aerodynamic center offset from the assigned reference point. It is therefore adopted here as the primary stability metric for comparison across thrust levels and tail configurations. Variations of aerodynamic derivatives with thrust coefficient on the complete aircraft configurations are given in Table 3.

The aircraft aerodynamic center is also known as the neutral point, that is the longitudinal coordinate of the moment reference center (normalized to the mean aerodynamic chord) that cancels the aircraft static stability. It physically represents the rearmost position of the center of gravity that keeps the aircraft longitudinally stable. Similarly to Eq. (3), it is evaluated as:

$$\bar{x}_N = \bar{x}_{ref} - \frac{dC_M}{dC_L} \tag{4}$$

where $\bar{x}_{ref} = 0.25$ and dC_M/dC_L is available in Table 3. Fig. 15 shows that the neutral point of the conventional tail configuration presented a step of 0.056 at positive thrust settings, moving from 0.461 to 0.517. Conversely, the T-tail presented a significant leap between prop-off and idling conditions. It practically provided the same value of the conventional tail in prop-off condition, with $\bar{x}_N = 0.47$. At $T_c = 0$ it jumped to 0.548 and then it linearly decreased with a rate of $(4.9 \pm 1.1)\%$ of the mean aerodynamic chord per unit T_c, with a 95% confidence interval. From the idling condition, the aircraft with the T-tail layout became less stable with increasing thrust levels.

Therefore, while both tail configurations exhibited the same longitudinal stability characteristics in prop-off condition, at $T_c = 0$ (idling) the T-tail was significantly more stable than the conventional tail. This was attributed to the relative vertical distance of the former to the wake of the propellers, while the latter was presumably always immersed in the propwash. Apparently, while in idling condition the wing aerodynamics was disturbed by the slowly rotating propellers, the T-tail was unaffected and kept its restoring action. For the same reason, at large thrust settings, with the wing immersed in the slipstream and the tailplane out of the wake, the T-tail contribution became relatively less important. Conversely, it can be argued that the wing and the conventional tail exhibited the same increment in effectiveness at positive thrust settings.

The evaluation of longitudinal control authority was made with the derivative $dC_M/d\delta_e$, also named elevator control power, indicating the rate of change of C_M per unit of elevator deflection δ_e. Wind tunnel runs of the complete aircraft configuration with the two tailplane layouts, initially performed with $\delta_e = 0°$, were repeated with $\delta_e = -10°$. The elevator control power was estimated as the incremental ratio:

$$\frac{dC_M}{d\delta_e} = \frac{C_M(\delta_e = -10°) - C_M(\delta_e = 0°)}{-10°} \tag{5}$$

where the evaluation was made at different angles of attack and thrust settings. Results are reported in Table 4. By performing a regression analysis at all angles of attack the lines of Fig. 16 were obtained. It is apparent that the conventional tail configuration exhibited a linear variation of the elevator control power, while the T-tail configuration was substantially unaffected in all conditions.

The baseline balance uncertainty propagated to a standard error of $\pm 0.0035\,\deg^{-1}$ for the individual elevator control power measurements.

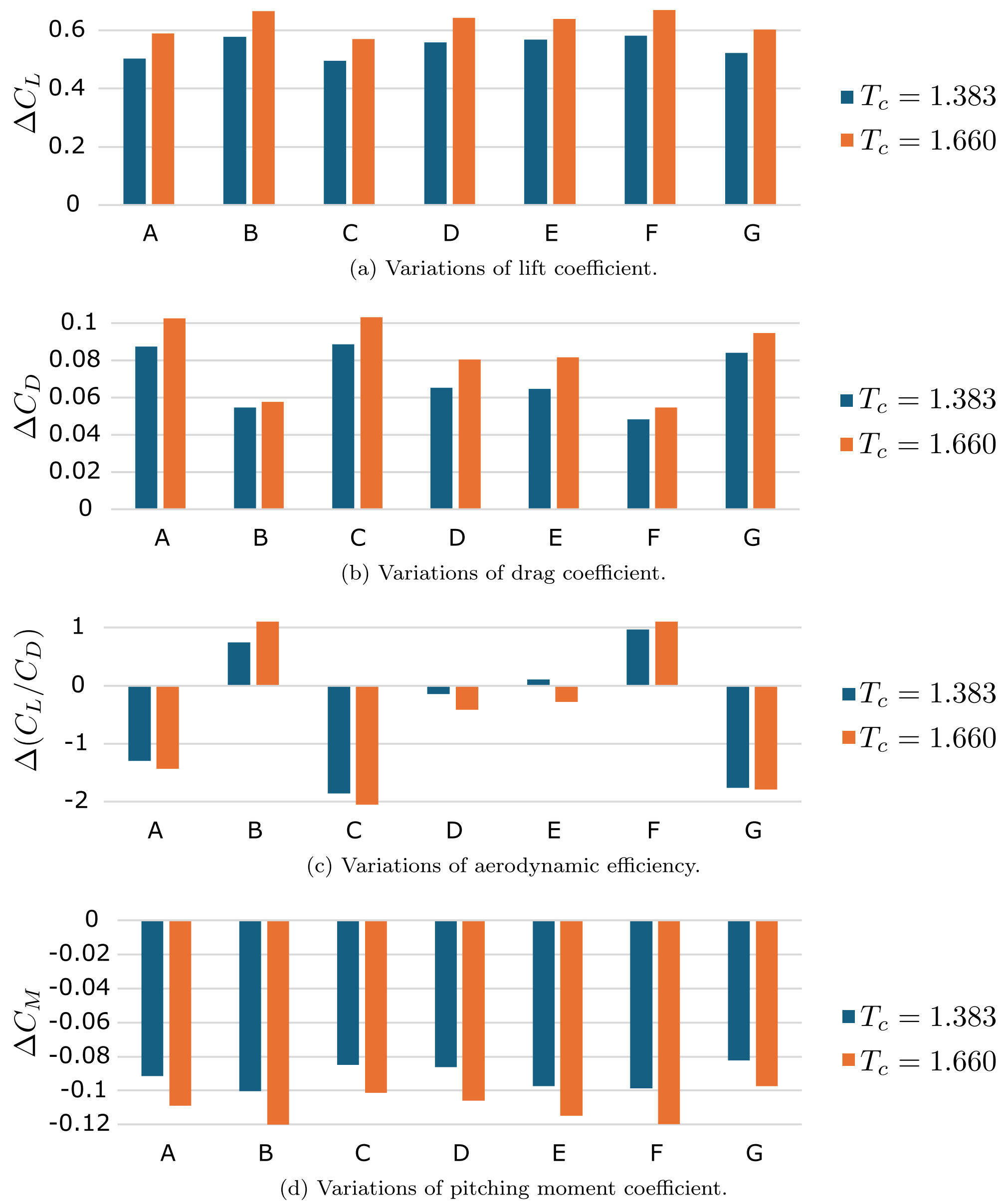

(a) Variations of lift coefficient.

(b) Variations of drag coefficient.

(c) Variations of aerodynamic efficiency.

(d) Variations of pitching moment coefficient.

Fig. 11. Impact of propellers position on the aerodynamic coefficients. Relative changes with respect to $T_c = 0$. Values at $\alpha_g = 5°$ (corrected $\alpha \approx 6°$).

To confirm the systematic trends observed in Fig. 16, a linear regression analysis of $\mathrm{d}C_M/\mathrm{d}\delta_e$ versus T_c was performed. For the conventional tail, the regression confirmed a highly significant ($p < .001$) linear augmentation of control authority, with the derivative $\mathrm{d}C_M/\mathrm{d}\delta_e$ becoming more negative at a rate of $(-0.0053 \pm 0.0009)\,\mathrm{deg}^{-1}$ per unit T_c (95% confidence interval). Conversely, the variations observed for the T-tail fell within the $\pm 0.0035\,\mathrm{deg}^{-1}$ measurement uncertainty band, confirming that its elevator control power remained statistically unaffected by the distributed propulsion.

Thus, stability and control characteristics exhibited some similarities. Distributed propulsion increased both longitudinal stability and control of the conventional tail configuration, where the neutral point moved aft by about 6% regardless of the positive thrust level and the elevator control power doubled in full power condition, from -0.009 to about -0.018. Conversely, the longitudinal stability decreased for the T-tail configuration, where the neutral point moved forward by about 8% in full power condition, while the elevator control power was not significantly altered by DEP operation.

Table 4
Elevator control power $\mathrm{d}C_M/\mathrm{d}\delta_e$ at different angles of attack and thrust settings. Values in deg^{-1}.

	Conventional tail		T-tail		
T_c	$\alpha = 0.6°$	$\alpha = 6.0°$	$\alpha = 0.6°$	$\alpha = 6.0°$	$\alpha = 9.1°$
prop-off	−0.0102	−0.0089	−0.0100	−0.0095	−0.0075
0	−0.0105	−0.0090	−0.0091	−0.0092	−0.0075
0.830	−0.0145	−0.0131	−0.0087	−0.0095	−0.0080
1.107	n.a.	n.a.	−0.0087	−0.0100	−0.0084
1.383	−0.0171	−0.0171	−0.0086	−0.0098	−0.0084
1.660	−0.0182	−0.0186	−0.0081	−0.0102	−0.0087

3.4. Considerations on longitudinal trim

The alteration of aircraft stability and control characteristics due to propellers blowing suggests that the effects of DEP on longitudinal trim are not intuitive. Generally, the elevator deflection δ_e is expected to

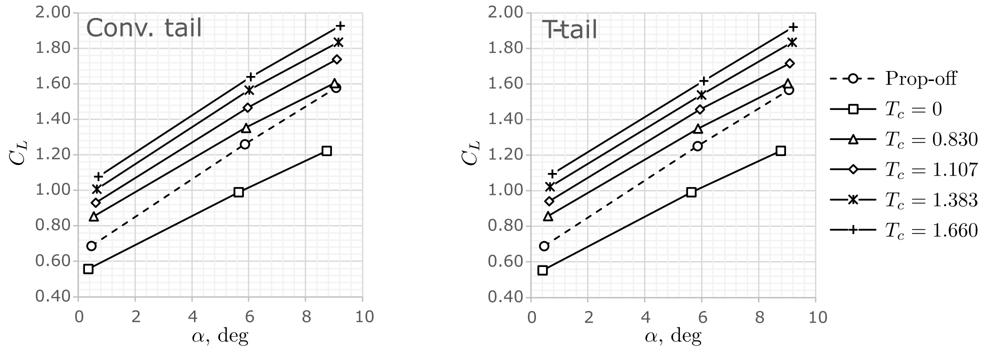

(a) Conventional aft tail (b) T-tail

Fig. 12. Lift coefficient vs. angle of attack for the two tailplane layouts. Elevator in neutral position ($\delta_e = 0°$).

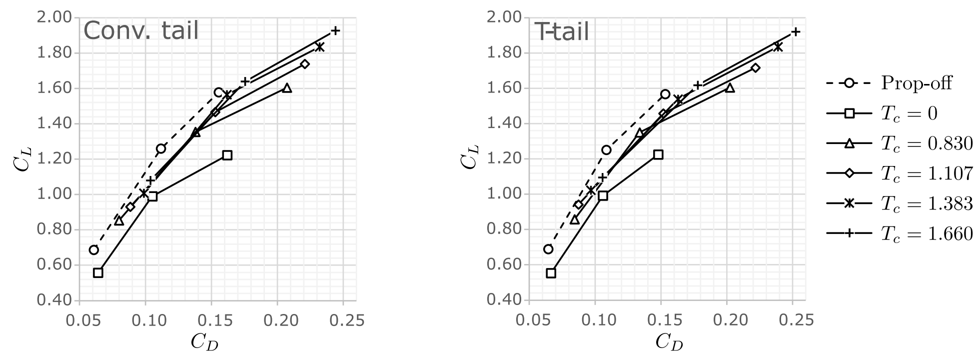

(a) Conventional aft tail (b) T-tail

Fig. 13. Drag polar for the two tailplane layouts. Elevator in neutral position ($\delta_e = 0°$).

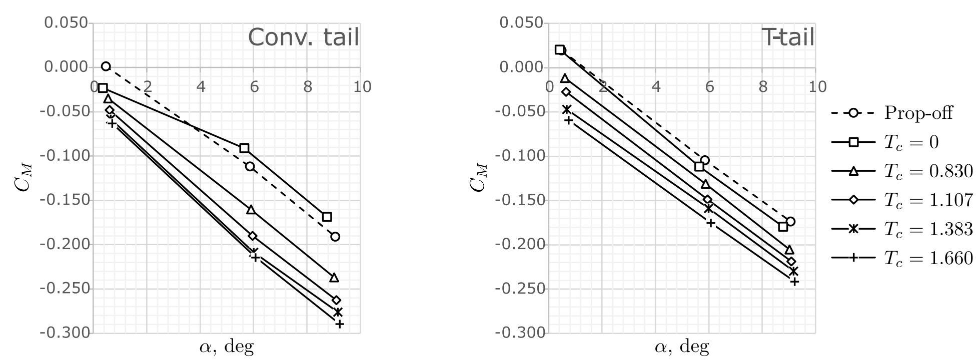

(a) Conventional aft tail (b) T-tail

Fig. 14. Pitching moment coefficient vs. angle of attack for the two tailplane layouts. Elevator in neutral position ($\delta_e = 0°$).

grow negative (pulling the stick) with the moment reference center $\overline{x}_{\text{ref}}$ moving forward and with increasing thrust coefficient T_c. However, it is here shown that, even by linearizing data, the combined effects due to distributed thrust with different tailplane configurations may provide non-monotonic trends.

The aircraft pitching moment coefficient is modeled as:

$$C_M = C_{M_0} + \frac{\mathrm{d}C_M}{\mathrm{d}\alpha}\alpha + \frac{\mathrm{d}C_M}{\mathrm{d}\delta_e}\delta_e \tag{6}$$

where C_{M_0} is the pitching moment coefficient at $\alpha = \delta_e = 0°$. To trim the aircraft Eq. (6) is solved for $C_M = 0$, providing the equilibrium elevator deflection angle:

$$\delta_{ee} = -\frac{C_{M_0} + \dfrac{\mathrm{d}C_M}{\mathrm{d}\alpha}\alpha}{\dfrac{\mathrm{d}C_M}{\mathrm{d}\delta_e}} \tag{7}$$

where the values of C_{M_0} are inferred as the intercept of the linearized data of Fig. 14 and the values of $\mathrm{d}C_M/\mathrm{d}\delta_e$ are taken from the regression lines of Fig. 16. The values of $\mathrm{d}C_M/\mathrm{d}\alpha$ could be taken from Table 3, but these would be only valid at $\overline{x}_{\text{ref}} = 0.25$. Therefore, to generalize the results at other reference points (i.e. center of gravity locations), the invariance of the neutral point is exploited here. The static stability margin SSM is defined by inverting Eq. (4):

$$\text{SSM} \equiv \frac{\mathrm{d}C_M}{\mathrm{d}C_L} = \overline{x}_{\text{ref}} - \overline{x}_{\text{N}} \tag{8}$$

where $\overline{x}_{\text{N}}$ is function of T_c only as in Fig. 15 and $\overline{x}_{\text{ref}}$ is assigned. From the SSM evaluated with Eq. (8), the values of $\mathrm{d}C_M/\mathrm{d}\alpha$ are calculated:

$$\frac{\mathrm{d}C_M}{\mathrm{d}\alpha} = \frac{\mathrm{d}C_M}{\mathrm{d}C_L}\cdot\frac{\mathrm{d}C_L}{\mathrm{d}\alpha} \tag{9}$$

where the lift gradient $\mathrm{d}C_L/\mathrm{d}\alpha$, available in Table 3, is invariant with $\overline{x}_{\text{ref}}$. Therefore, Eq. (7) can be applied to estimate the equilibrium ele-

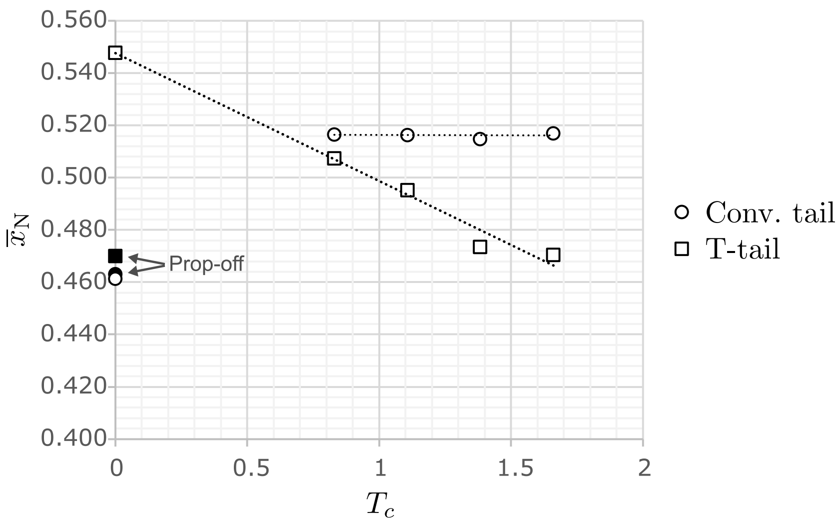

Fig. 15. Neutral point vs. thrust coefficient.

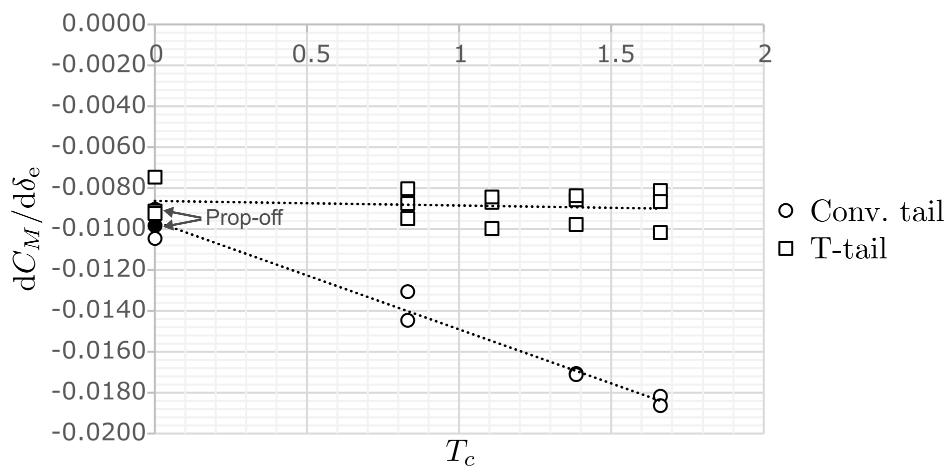

Fig. 16. Elevator control power vs. thrust coefficient.

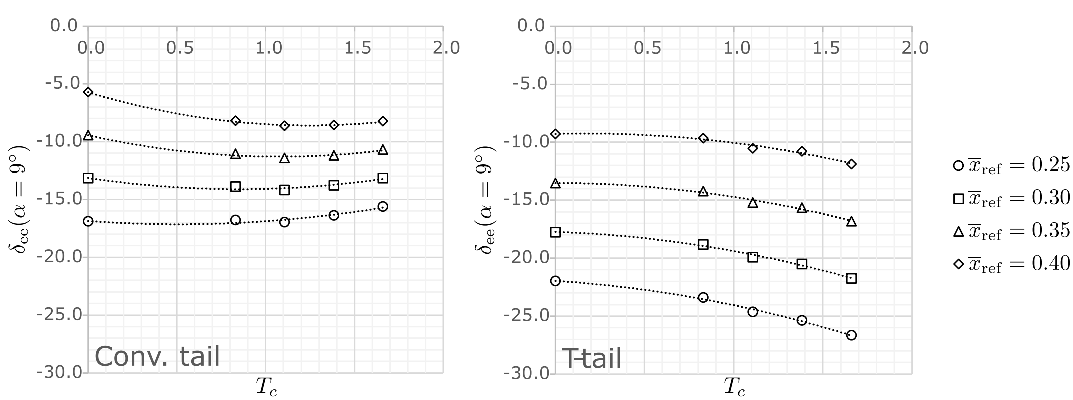

(a) Conventional aft tail (b) T-tail

Fig. 17. Equilibrium elevator deflection angle at $\alpha = 9°$ vs. thrust coefficient for the two tailplane layouts at different moment reference points.

vator deflection angle δ_{ee} at any corrected angle of attack α within the investigated range. As an application case, Eq. (7) is solved for the highest investigated value of angle of attack ($\alpha = 9°$) and a reference point $\overline{x}_{ref}$ varying from 0.25 to 0.40 with 0.05 step, representing typical center of gravity positions. Extrapolation is possible as long as the linearization of aerodynamic data is feasible, i.e. in attached flow conditions. Results are shown in Fig. 17 for both conventional and T-tail configurations.

Even by linearizing the available data, the combination of stability and control characteristics under the influence of propellers slipstream of different intensity is such that the variation of the required elevator deflection angle δ_{ee} for longitudinal equilibrium is nonlinear with the thrust coefficient T_c. The best-fit lines suggest that δ_{ee} exhibits a mild quadratic dependence on T_c. For both tail configurations, advancing the reference point would require a larger pull-up deflection, while increasing the thrust coefficient has different effects depending on the slipstream impingement on the horizontal tail.

Since the conventional tail was immersed in the propellers' slipstream, the amplified elevator control power is largely sufficient to trim the aircraft at $\alpha = 9°$ for all the values of T_c and $\bar{x}_{\text{ref}}$, despite the increased pitch-down tendency. On top of that, estimated values of δ_{ee} are not always decreasing with T_c. For $\bar{x}_{\text{ref}} = 0.25$ the required elevator deflection angle at full power is even less negative than low-power conditions, requiring a slight relaxation of the stick-pull force. This means that the elevator control power derivative $\mathrm{d}C_M/\mathrm{d}\delta_{\text{e}}$ grows with T_c faster than the stability derivative $\mathrm{d}C_M/\mathrm{d}\alpha$, which is directly proportional to the static margin $\mathrm{d}C_M/\mathrm{d}C_L$ and the lift curve slope $\mathrm{d}C_L/\mathrm{d}\alpha$. The former is constant for a given $\bar{x}_{\text{ref}}$, whereas the latter grows with T_c. This also explains the change of the curves slope in Fig. 17a: the second term of the numerator of Eq. (7) grows when T_c increases and $\bar{x}_{\text{ref}}$ decreases (i.e. $\mathrm{d}C_M/\mathrm{d}C_L$ increases), whereas the denominator increases only with T_c.

Conversely, since the T-tail was out of the propwash, the required negative deflection angle also increases with the thrust coefficient. The control power derivative $\mathrm{d}C_M/\mathrm{d}\delta_{\text{e}}$ stays constant with T_c and the slope of the curves in Fig. 17b is entirely shaped by the stability derivative $\mathrm{d}C_M/\mathrm{d}\alpha$, which grows with increasing T_c and reducing $\bar{x}_{\text{ref}}$.

There is at least one data point that raises a concern for the T-tail configuration. At $\bar{x}_{\text{ref}} = 0.25$ and $T_c = 1.66$, a $\delta_{\text{ee}} \approx -26.5°$ should be set. However, this is a value very close to the usual elevators end-stop, meaning that if the investigated conditions hold in flight, the aircraft could not be trimmed in full-power conditions at angles of attack higher than 9°, making low-speed operations—like an initial climb—difficult.

3.5. Incremental effects

The previous discussion on aircraft equilibrium, stability, and control during DEP operation implies that the design of the horizontal tail strongly depends on the its distance from the distributed propellers' wake. In fact, even with similar volumetric ratios, the configurations investigated in this work exhibited largely different stability and control characteristics. They may be considered as limit cases: the conventional tail immersed in the propwash and the T-tail out. An intermediate behavior is expected with different layouts (e.g. low wing or cruciform tail), although nonlinear effects are hard to predict and should be carefully investigated.

It could be argued that the impact of DEP should have been evaluated with respect to the prop-off configuration with frame, taking the unpowered condition as reference, but accounting for the aerodynamic interference of the support structure for a fair comparison with powered tests. However, it is unlikely that a full-scale DEP-powered aircraft could disengage all the motors in flight, bringing the wing to a configuration similar to the prop-off condition investigated here. Therefore, it seemed reasonable to compare the aero-propulsive effects with respect to the idling conditions, which could be met in a descent phase.

To provide guidelines to aircraft designers, the aerodynamic data of the complete aircraft configurations are presented here as incremental effects with thrust coefficient. Data distributions were linearized where possible and a complete set of equations is derived for each tailplane configuration. Readers involved in similar designs may promptly use this model to perform a preliminary analysis before setting up computational intensive high-fidelity simulations or an expensive wind tunnel test campaign.

Figs. 18 to 20 present increments of lift, drag, and pitching moment coefficient, respectively. Regression lines yielded $R^2 > 0.99$, indicating that a linear model was a good fit. However, for a given T_c only some of the increments were linearly affected by the corrected angle of attack α. On the conventional tail configuration the ΔC_M increased significantly between $\alpha = 0°$ and $\alpha = 6°$, while its magnitude was slightly reduced between $\alpha = 6°$ and $\alpha = 9°$. Similarly, the ΔC_M on the T-tail configuration exhibited a nonlinear variation with α, but in the opposite direction. This is a further confirmation that the conventional tail was immersed in the propwash at moderate angles of attack, while the vertical separation between the T-tail and the slipstream increased with the angle of attack.

Therefore, the models for lift and drag coefficient are assumed linear with both thrust coefficient and angle of attack, whereas the pitching moment coefficient is modeled as linear with thrust coefficient and quadratic with the angle of attack. The models for increments in aerodynamic coefficients are:

$$\Delta C_L = \frac{\mathrm{d}\Delta C_L}{\mathrm{d}T_c} T_c = \left(a_0 + a_1\alpha\right) T_c \tag{10}$$

$$\Delta C_D = \frac{\mathrm{d}\Delta C_D}{\mathrm{d}T_c} T_c = \left(b_0 + b_1\alpha\right) T_c \tag{11}$$

$$\Delta C_M = \frac{\mathrm{d}\Delta C_M}{\mathrm{d}T_c} T_c = \left(c_0 + c_1\alpha + c_2\alpha^2\right) T_c \tag{12}$$

where the values of $\mathrm{d}\Delta(\cdot)/\mathrm{d}T_c$ are the slopes of the regression lines of Figs. 18 to 20. They have been reported in Table 5. By applying the polynomial regression on these values, the coefficients $a_0, a_1, b_0, b_1, c_0, c_1, c_2$ are obtained. Values of such coefficients are substituted in (10) to (12) for each tail configuration.

For the conventional tail configuration, the incremental coefficients are:

$$\Delta C_L = (0.3203 + 0.0139\alpha)T_c \tag{13}$$

$$\Delta C_D = (0.0217 + 0.0033\alpha)T_c \tag{14}$$

$$\Delta C_M = \left(-0.0117 - 0.0200\alpha + 0.0014\alpha^2\right)T_c \tag{15}$$

whereas for the T-tail configuration, the incremental coefficients are:

$$\Delta C_L = (0.3313 + 0.0112\alpha)T_c \tag{16}$$

$$\Delta C_D = (0.0173 + 0.0049\alpha)T_c \tag{17}$$

$$\Delta C_M = \left(-0.0486 + 0.0041\alpha - 0.0003\alpha^2\right)T_c \tag{18}$$

with α expressed in deg. Eqs. (13) to (15) are validated against the data set shown by the markers of Figs. 18a, 19a, and 20a, respectively, in Table 6. Similarly, Eqs. (16) to (18) are validated against the data in Figs. 18b, 19b, and 20b, respectively, in Table 7. Despite some large discrepancies in a few conditions, the average error is below 5% for the ΔC_L and ΔC_D of the conventional configuration as well as for the ΔC_L of the T-tail configuration. The other increments are predicted with an average error of about 10% with respect to wind tunnel data. Therefore, the provided equations can be confidently used for the preliminary estimation of distributed propellers indirect effects. Their validity is limited to the investigated range of angles of attack (α from 0° to 9°) and thrust coefficients ($T_c \leq 1.66$).

3.6. Transferability of results and implications for take-off performance

The drag increments ΔC_D reported here were obtained at Reynolds numbers representative of wind-tunnel testing conditions ($Re \approx 2 \times 10^5$). As stated in Section 2.2, the combination of high-RPM propeller slipstream and transitional strips provided a turbulent boundary layer on the model. As a consequence, it is believed that the measured drag increments ΔC_D were not affected by the low-Re viscous artifacts that would otherwise limit the transferability of wind-tunnel results.

While absolute drag coefficients are known to decrease approximately logarithmically with Reynolds number, the DEP-induced drag increment was dominated by the inviscid slipstream effect on induced drag, which scaled with ΔC_L rather than with viscous parameters. A first-order transferability estimate can be obtained by scaling only the friction-driven portion of ΔC_D with a fully turbulent skin-friction correlation. Based on the present scale and speed ratios, the full-scale Reynolds number is expected to be about 30 times higher than the

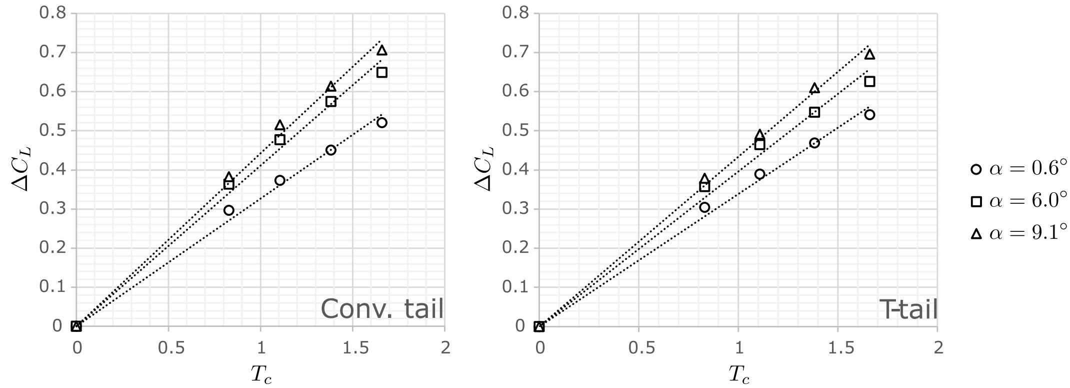

(a) Conventional aft tail (b) T-tail

Fig. 18. Incremental effects of DEP on the lift coefficient for the complete aircraft configurations as function of thrust coefficient and corrected angle of attack.

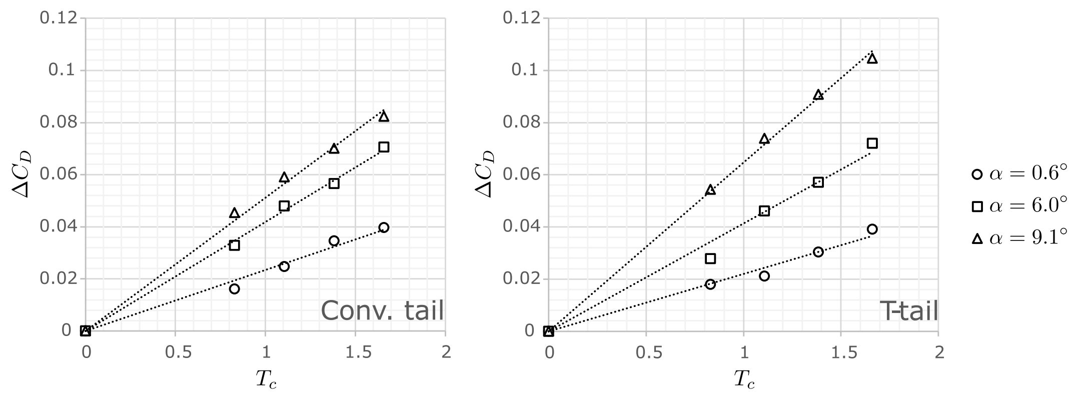

(a) Conventional aft tail (b) T-tail

Fig. 19. Incremental effects of DEP on the drag coefficient for the complete aircraft configurations as function of thrust coefficient and corrected angle of attack.

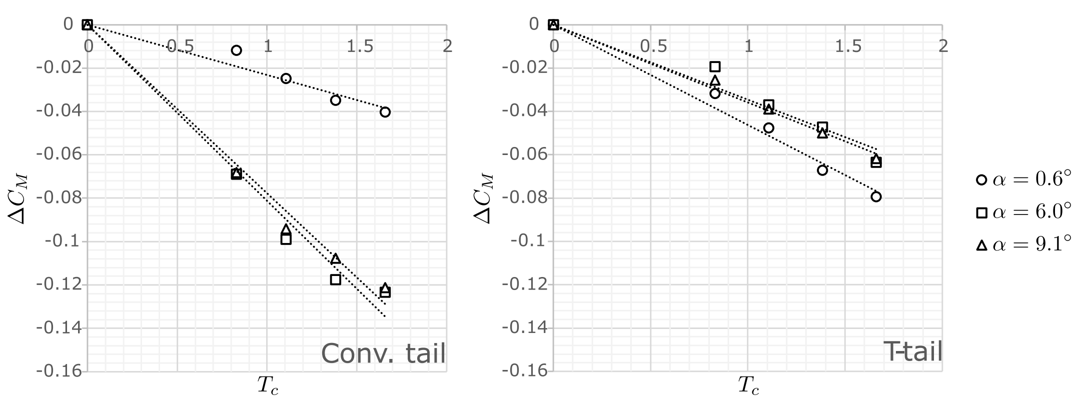

(a) Conventional aft tail (b) T-tail

Fig. 20. Incremental effects of DEP on the pitching moment coefficient for the complete aircraft configurations as function of thrust coefficient and corrected angle of attack.

model's value. By applying the Prandtl-Schlichting turbulent correlation, the full-scale skin-friction coefficient is expected to be about one-half of the wind-tunnel value, so the measured drag increments should be regarded as conservative when interpreted as total increments, while the pressure-driven DEP effects are expected to transfer more directly.

Both ΔC_L and ΔC_D, and therefore the DEP-induced change in aerodynamic efficiency $\Delta(C_L/C_D)$, are considered reliable at full-scale Reynolds numbers. The regression-based correlations of these increments with thrust coefficient and angle of attack derived from the present dataset are therefore directly applicable to preliminary design and sizing analyses, pending validation with high-fidelity CFD or flight-test data at a later design stage.

The measured increase in $C_{L_{\max}}$ due to DEP operation implies a lower lift-off speed, which tends to shorten the take-off ground roll. However, the simultaneous increase in C_D documented here partially offsets this benefit, since the higher drag reduces the net accelerating force along the runway. The balance between these two competing effects cannot be resolved from aerodynamic data alone and requires an integrated take-off performance analysis, identified here as a topic for future work.

Table 5
Values of the slope of the regression lines of Figs. 18 to 20.

	Conventional tail			T-tail		
α (deg)	$\mathrm{d}\Delta C_L/\mathrm{d}T_c$	$\mathrm{d}\Delta C_D/\mathrm{d}T_c$	$\mathrm{d}\Delta C_M/\mathrm{d}T_c$	$\mathrm{d}\Delta C_L/\mathrm{d}T_c$	$\mathrm{d}\Delta C_D/\mathrm{d}T_c$	$\mathrm{d}\Delta C_M/\mathrm{d}T_c$
0.6	0.326	0.023	−0.023	0.339	0.022	−0.046
6.0	0.411	0.042	−0.081	0.396	0.041	−0.035
9.1	0.442	0.051	−0.078	0.434	0.065	−0.036

Table 6
Validation of the Eqs. (13) to (15). Deviations from wind tunnel data.

α (deg)	T_c	ΔC_L	ΔC_L err.	ΔC_D	ΔC_D err.	ΔC_M	ΔC_M err.
0.6	0.830	0.273	−7.9%	0.020	21.9%	−0.019	61.3%
0.6	1.107	0.364	−2.5%	0.026	6.3%	−0.026	3.3%
0.6	1.383	0.455	0.9%	0.033	−5.6%	−0.032	−8.3%
0.6	1.660	0.546	4.7%	0.039	−1.0%	−0.038	−4.4%
6.0	0.830	0.335	−7.8%	0.034	4.5%	−0.067	−2.4%
6.0	1.107	0.447	−6.3%	0.046	−4.4%	−0.090	−9.2%
6.0	1.383	0.558	−2.8%	0.057	1.0%	−0.112	−4.5%
6.0	1.660	0.670	3.1%	0.069	−2.7%	−0.135	9.2%
9.1	0.830	0.371	−3.0%	0.043	−0.7%	−0.064	−5.6%
9.1	1.107	0.494	−4.2%	0.057	−0.4%	−0.086	−8.7%
9.1	1.383	0.618	0.5%	0.071	0.2%	−0.107	−0.3%
9.1	1.660	0.741	4.9%	0.085	0.4%	−0.129	6.3%
avg. abs. error		ΔC_L	4.1%	ΔC_D	4.1%	ΔC_M	10.3%

Table 7
Validation of the Eqs. (16) to (18). Deviations from wind tunnel data.

α (deg)	T_c	ΔC_L	ΔC_L err.	ΔC_D	ΔC_D err.	ΔC_M	ΔC_M err.
0.6	0.830	0.281	−7.9%	0.017	−6.4%	−0.038	20.4%
0.6	1.107	0.374	−3.8%	0.022	5.9%	−0.051	7.3%
0.6	1.383	0.467	−0.3%	0.028	−7.8%	−0.064	−5.0%
0.6	1.660	0.561	3.7%	0.034	−14.3%	−0.077	−3.4%
6.0	0.830	0.331	−7.5%	0.039	38.5%	−0.029	47.6%
6.0	1.107	0.441	−5.2%	0.051	11.8%	−0.038	3.7%
6.0	1.383	0.551	0.6%	0.064	12.5%	−0.048	1.4%
6.0	1.660	0.661	5.6%	0.077	7.2%	−0.057	−9.6%
9.1	0.830	0.359	−5.2%	0.051	−6.1%	−0.030	15.9%
9.1	1.107	0.479	−2.4%	0.068	−7.9%	−0.040	2.0%
9.1	1.383	0.599	−1.9%	0.085	−6.3%	−0.050	−0.8%
9.1	1.660	0.718	3.2%	0.102	−2.3%	−0.060	−3.6%
avg. abs. error		ΔC_L	3.9%	ΔC_D	10.6%	ΔC_M	10.1%

3.7. Limitations

This study has several limitations that should be considered when interpreting the results.

- Dynamic and unsteady aerodynamic derivatives were not measured; while the observed changes in $\mathrm{d}C_M/\mathrm{d}\alpha$ suggest corresponding effects on pitch stiffness and short-period response, these were not directly quantified and remain a topic for a dedicated investigation.
- The tests were performed at a fixed Reynolds number well below full-scale flight conditions, consistent with the 1:12 geometric scale of the model; while thrust-coefficient similarity was matched (Section 2.2), the resulting Reynolds number mismatch may affect boundary layer behavior and the transferability of absolute coefficient values to the full-scale aircraft, even though the qualitative trends with thrust and tail configuration are expected to hold.
- All tests were conducted at a single flap deflection ($\delta_f = 15°$, representative of take-off configuration); the sensitivity of the reported stability and control derivatives to other flap settings (e.g., landing configuration) was not investigated and warrants further testing.
- The considerations on longitudinal trim assume that the pitching moment coefficient can be modeled as the sum of individual and separate effects. Similarly, the assumed invariance of the neutral point implicitly requires a static margin that is constant at any attitude, depending only on the reference point location. While acceptable for preliminary design, experimental tests over a larger range of angles of attack are required to validate this assumption.
- Extrapolation of the present wind-tunnel results to full-scale aircraft behavior should be made with caution, given the combined effects of Reynolds number mismatch, the simplified propulsive frame installation (detached from the airframe), and the exclusion of direct propulsive contributions (thrust line and propeller normal force moments) from the balance measurements, as noted in Section 2.3.

4. Conclusions

Wind-tunnel tests on a scaled 19-seat commuter aircraft model were performed to quantify the indirect aero-propulsive effects of a leading-edge distributed high-lift propeller system on longitudinal static stability and control characteristics. Despite the growing body of DEP literature, the overwhelming majority of published works focuses on lift augmentation and drag penalties, leaving the pitching-moment behavior, static-margin shifts, and elevator control authority under powered conditions largely unaddressed. The present experimental campaign directly targets this gap, providing the first comprehensive, measurement-based characterization of these effects for a commuter-class aircraft with alternative horizontal tail configurations. Two tail layouts, a conventional aft tail and a T-tail, were investigated at a take-off flap setting over a range of typical thrust coefficients and angles of attack. The main conclusions are here drawn.

- DEP operation significantly increased the pitch-down moment of the wing-body combination, with the pitching moment C_M at low angle of attack nearly doubling from approximately −0.1 to −0.2 at full thrust. This result demonstrates that the sole characterization of lift and drag increments due to DEP is insufficient for aircraft design: the concurrent and substantial modification of the pitching moment must be accounted for to correctly assess trim, stability, and control authority.
- The two tail configurations responded differently to the DEP-induced slipstream, revealing that the horizontal tail position relative to the propeller wake is a first-order design parameter that is absent from most existing DEP design frameworks. The conventional aft tail, immersed in the propwash, experienced increased local dynamic pressure and reduced downwash gradient, resulting in a nearly constant shift in static margin of 6% for all positive thrust settings, with the neutral point estimated at approximately 52% of the mean aerodynamic chord. The T-tail, located outside the slipstream, showed a linear reduction in static margin with thrust coefficient, with the neutral point moving forward at a rate of approximately 5% per unit T_c.
- Elevator control power $\mathrm{d}C_M/\mathrm{d}\delta_e$ approximately doubled for the conventional tail configuration at full thrust, increasing from $-0.009\,\mathrm{deg}^{-1}$ at idle to approximately $-0.018\,\mathrm{deg}^{-1}$ at $T_c = 1.66$, while it remained substantially unaffected by DEP operation for the T-tail layout. This asymmetry between configurations, which would be invisible to any analysis restricted to lift and drag, has direct consequences for tail sizing and trim authority.
- The combined effect of increased stability and amplified control power allowed the conventional tail configuration to trim the aircraft up to $\alpha = 9°$ for all investigated thrust levels and center-of-gravity positions. The T-tail layout, conversely, required elevator

deflections approaching the assumed stop value at full power and forward center-of-gravity positions, indicating potential trim limitations in low-speed DEP-powered operations that would not be anticipated from lift-only assessments.

The results demonstrate that restricting DEP analysis to lift and drag increments, as is common practice in the current literature, leads to an incomplete and potentially misleading picture of the aero-propulsive interaction. Pitching moment, static margin, and elevator control power are all substantially affected by DEP operation, and their sensitivity to horizontal tail placement relative to the propeller slipstream is large enough to determine whether a given configuration is trimmable throughout its operating envelope. These findings provide experimentally grounded guidance for horizontal tail sizing and placement in commuter-class DEP aircraft, and establish a reference dataset for the validation of higher-fidelity computational and analytical methods.

Preliminary sizing of horizontal tail for DEP-powered aircraft configurations can be promptly performed with the presented model of incremental effects and the derived measures of longitudinal stability and control derivatives. Future work should experimentally assess the impact of distributed propellers on the lateral-directional characteristics of the same model, providing a complete picture of DEP influence over commuter aircraft aerodynamics, stability, and control.

CRediT authorship contribution statement

Danilo Ciliberti: Writing – original draft, Validation, Software, Methodology, Formal analysis, Data curation, Conceptualization; **Fabrizio Nicolosi:** Writing – review & editing, Visualization, Supervision, Project administration, Investigation, Funding acquisition.

Funding

This research was funded by the Italian PROSIB (Propulsione e Sistemi Ibridi per velivoli ad ala fissa e rotante—Hybrid Propulsion and Systems for fixed and rotary wing aircraft) project PNR 2015–2020 ARS01_00297 lead by Leonardo S.p.A.

Declaration of competing interest

The authors declare that they have no known competing financial interests or personal relationships that could have appeared to influence the work reported in this paper.

Acknowledgments

The authors are grateful to Domenico Idioma, who contributed to this work as a Master's student, for his support during wind tunnel tests.

Data availability

Data will be made available on request.

References

[1] A.S. Gohardani, G. Doulgeris, R. Singh, Challenges of future aircraft propulsion: a review of distributed propulsion technology and its potential application for the all electric commercial aircraft, Prog. Aerosp. Sci. 47 (5) (2011) 369–391. https://doi.org/10.1016/j.paerosci.2010.09.001
[2] H.D. Kim, A.T. Perry, P.J. Ansell, A review of distributed electric propulsion concepts for air vehicle technology, in: AIAA/IEEE Electric Aircraft Technologies Symposium, 2018. https://doi.org/10.2514/6.2018-4998
[3] S. Sahoo, X. Zhao, K. Kyprianidis, A review of concepts, benefits, and challenges for future electrical propulsion-based aircraft, Aerospace 7 (4) (2020). https://doi.org/10.3390/aerospace7040044
[4] A.M. Stoll, E.V. Stilson, J. Bevirt, P.P. Pei, Conceptual design of the Joby S2 electric VTOL PAV, in: 14th AIAA Aviation Technology, Integration, and Operations Conference, AIAA AVIATION Forum, American Institute of Aeronautics and Astronautics, 2014. https://doi.org/10.2514/6.2014-2407
[5] M.D. Patterson, N.K. Borer, B. German, A simple method for high-lift propeller conceptual design, in: 54th AIAA Aerospace Sciences Meeting, January, 2016. https://doi.org/10.2514/6.2016-0770
[6] D. Ciliberti, P. Della Vecchia, V. Orticalco, F. Nicolosi, Aero-propulsive interactions between UAV wing and distributed propellers due to their relative position, Drones 7 (1) (2023) 49. https://doi.org/10.3390/drones7010049
[7] C. Pornet, C. Gologan, P.C. Vratny, A. Seitz, O. Schmitz, A.T. Isikveren, M. Hornung, Methodology for sizing and performance assessment of hybrid energy aircraft, J. Aircr. 52 (1) (2014) 341–352. https://doi.org/10.2514/1.c032716
[8] C. Pornet, A.T. Isikveren, Conceptual design of hybrid-electric transport aircraft, Prog. Aerosp. Sci. 79 (2015) 114–135. https://doi.org/10.1016/j.paerosci.2015.09.002
[9] F. Orefice, P. Della Vecchia, D. Ciliberti, F. Nicolosi, Preliminary design to fulfil future market demand of electric aircraft, Int. Rev. Aerosp. Eng. 14 (6) (2021). https://doi.org/10.15866/irease.v14i6.20814
[10] D. Ciliberti, P. Della Vecchia, V. Memmolo, F. Nicolosi, G. Wortmann, F. Ricci, The enabling technologies for a quasi-zero emissions commuter aircraft, Aerospace 9 (6) (2022) 319. https://doi.org/10.3390/aerospace9060319
[11] A.M. Stoll, Comparison of CFD and experimental results of the LEAPTech distributed electric propulsion blown wing, in: 15th AIAA Aviation Technology, Integration, and Operations Conference, American Institute of Aeronautics and Astronautics, Reston, Virginia, 2015, pp. 22–26. https://doi.org/10.2514/6.2015-3188
[12] K.A. Deere, S.A. Viken, M.B. Carter, J.K. Viken, J.M. Derlaga, A.M. Stoll, Comparison of high-fidelity computational tools for wing design of a distributed electric propulsion aircraft, in: 35th AIAA Applied Aerodynamics Conference, 2017. https://doi.org/10.2514/6.2017-3925
[13] K. Wang, Z. Zhou, X. Zhu, X. Xu, Aerodynamic design of multi-propeller/wing integration at low Reynolds numbers, Aerosp. Sci. Technol. 84 (2019). https://doi.org/10.1016/j.ast.2018.07.023
[14] P. Bevilaqua, C. Yam, Propulsive efficiency of wake ingestion, J. Propuls. Power 36 (4) (2020) 517–526. https://doi.org/10.2514/1.B37695
[15] E. Valencia, V. Alulema, D. Rodriguez, P. Laskaridis, I. Roumeliotis, Novel fan configuration for distributed propulsion systems with boundary layer ingestion on an hybrid wing body airframe, Therm. Sci. Eng. Prog. 18 (2020). https://doi.org/10.1016/j.tsep.2020.100515
[16] C. Xue, Z. Zhou, Inverse aerodynamic design for DEP propeller based on desired propeller slipstream, Aerosp. Sci. Technol. 102 (2020). https://doi.org/10.1016/j.ast.2020.105820
[17] Y. Lei, W.-j. Yang, Y.-y. Huang, Aerodynamic performance of distributed electric propulsion with wing interaction, J. Zhejiang Univ.-SCI. A 23 (1) (2022) 27–39. https://doi.org/10.1631/jzus.A2100192
[18] M. Schollenberger, B. Kirsch, T. Lutz, E. Krämer, J. Friedrichs, Aerodynamic interactions between distributed propellers and the wing of an electric commuter aircraft at cruise conditions, CEAS Aeronaut. J. 15 (2) (2024) 255–267. https://doi.org/10.1007/s13272-023-00706-6
[19] G. Wang, Z. Zhou, Q. Zhao, B. Li, M. Li, R. Wang, Analytical propulsion-Aerodynamic coupling model and validation for distributed propulsion wing lift enhancement configuration, Aerosp. Sci. Technol. 176 (2026). https://doi.org/10.1016/j.ast.2026.112012
[20] B. Sarikaya, T. Lutz, E. Krämer, Design improvement of a distributed propulsion system in cruise using numerical simulations, J. Aircr. (2026) 1–16. https://doi.org/10.2514/1.C038893
[21] N.K. Borer, M.D. Patterson, J.K. Viken, M.D. Moore, J. Bevirt, A.M. Stoll, A.R. Gibson, Design and performance of the NASA SCEPTOR distributed electric propulsion flight demonstrator, in: 16th AIAA Aviation Technology, Integration, and Operations Conference, American Institute of Aeronautics and Astronautics, Reston, Virginia, 2016. https://doi.org/10.2514/6.2016-3920
[22] E. Nguyen Van, D. Alazard, C. Döll, P. Pastor, Co-design of aircraft vertical tail and control laws using distributed electric propulsion, IFAC-Pap. 52 (12) (2019) 514–519. https://doi.org/10.1016/j.ifacol.2019.11.295
[23] X. Fei, B. German, M.D. Patterson, Exploring the effects of installation geometry in high-lift propeller systems, in: 2018 AIAA Aerospace Sciences Meeting, American Institute of Aeronautics and Astronautics, Kissimmee, Florida, 2018. https://doi.org/10.2514/6.2018-0277
[24] J.L. Freeman, G.T. Klunk, Dynamic flight simulation of spanwise distributed electric propulsion for directional control authority, in: 2018 AIAA/IEEE Electric Aircraft Technologies Symposium, American Institute of Aeronautics and Astronautics, Reston, Virginia, 2018. https://doi.org/10.2514/6.2018-4997
[25] D. Keller, Towards higher aerodynamic efficiency of propeller-driven aircraft with distributed propulsion, CEAS Aeronaut. J. 12 (4) (2021) 777–791. https://doi.org/10.1007/s13272-021-00535-5
[26] D. Keller, Numerical study on lift augmentation via distributed propulsion for a propeller-driven regional transport aircraft in landing configuration, CEAS Aeronaut. J. 17 (2) (2026) 553–566. https://doi.org/10.1007/s13272-025-00863-w
[27] K.A. Deere, B.L. Owens, J.K. Aiken, B.S. Stoll, Computational analysis of a wing designed for the X-57 distributed electric propulsion aircraft, in: 35th AIAA Applied Aerodynamics Conference, 2017, pp. 3923. https://doi.org/10.2514/6.2017-3923
[28] J.R. Serrano, A.O. Tiseira, L.M. García-Cuevas, P. Varela, Computational study of the propeller position effects in wing-mounted, distributed electric propulsion with boundary layer ingestion in a 25 kg remotely piloted aircraft, Drones 5 (3) (2021). https://doi.org/10.3390/drones5030056
[29] D. de Rosa, E. Morales Tirado, G. Mingione, Parametric investigation of a distributed propulsion system on a regional aircraft, Aerospace 9 (4) (2022). https://doi.org/10.3390/aerospace9040176
[30] R. de Vries, M. van Arnhem, T. Sinnige, R. Vos, L.L.M. Veldhuis, Aerodynamic interaction between propellers of a distributed-propulsion system in forward flight,

Aerosp. Sci. Technol. 118 (2021) 107009. https://doi.org/10.1016/j.ast.2021.107009

[31] A. Savino, A. Zanotti, Aerodynamic interaction between wing and propeller in eVTOL airplane mode flight condition, CEAS Aeronaut. J. (2025). https://doi.org/10.1007/s13272-025-00871-w

[32] L. Li, L. Qiao, J. Xu, J. Bai, Improved aerodynamic-propulsion interaction model for distributed-electric-propulsion system and its integration in sizing for hybrid-electric distributed-propulsion aircraft, Aerosp. Sci. Technol. 170 (2026) 111519. https://doi.org/10.1016/j.ast.2025.111519

[33] S. Chen, Z. Guo, D. Liu, D. Hu, B. Zhu, Aerodynamic optimization of wings under slipstream effects for a distributed propulsion system, Aerosp. Sci. Technol. 175 (2026). https://doi.org/10.1016/j.ast.2026.111929

[34] M. Hoogreef, J.S.E. Soikkeli, Flight dynamics and control assessment for differential thrust aircraft in engine inoperative conditions including aero-propulsive effects, CEAS Aeronaut. J. 13 (3) (2022). https://doi.org/10.1007/s13272-022-00591-5

[35] D. Kim, Y. Lee, S. Oh, Y. Park, J. Choi, D. Park, Aerodynamic analysis and static stability analysis of manned/unmanned distributed propulsion aircrafts using actuator methods, J. Wind Eng. Ind. Aerodyn. 214 (2021) 104648. https://doi.org/10.1016/j.jweia.2021.104648

[36] S. Cacciola, L. Bottá, C.E.D. Riboldi, L. Trainelli, Identification of the impact of blowing on the aerodynamic model of an airplane with distributed electric propulsion, in: 34th ICAS Congress, 2024.

[37] M. Schollenberger, M. Firnhaber Beckers, T. Lutz, E. Krämer, D. Bergmann, J. Denzel, A. Strohmayer, O. Pfeifle, W. Fichter, Cruise flight simulation of distributed propulsion and wingtip-mounted propeller aircraft and their validation with in-flight measurement data, CEAS Aeronaut. J. (2025). https://doi.org/10.1007/s13272-025-00869-4

[38] J. Qin, Z. Zhou, G. Yang, Z. Shao, J. Zong, Aero-propulsive coupling modeling and dynamic stability analysis of distributed electric propulsion tandem-wing UAV with rapid ascent capability, Aerosp. Sci. Technol. 153 (2024). https://doi.org/10.1016/j.ast.2024.109406

[39] J. Wei, B. Lu, Z. Zha, Q. Li, Aerodynamic modeling of a distributed propulsion system with coupling between propellers, wing, and flaps, Aerosp. Sci. Technol. 166 (2025). https://doi.org/10.1016/j.ast.2025.110538

[40] D. Ciliberti, G. Buonagura, F. Nicolosi, Longitudinal wind tunnel tests of the PROSIB 19-Pax airplane, Appl. Sci. 13 (21) (2023). https://doi.org/10.3390/app132111928

[41] J.B. Barlow, W.H. Rae, A. Pope, Low-Speed Wind Tunnel Testing, Wiley, New York, 1999.

[42] D. Ciliberti, F. Nicolosi, Design, analysis, and testing of a scaled propeller for an innovative regional turboprop aircraft, Aerospace 9 (5) (2022) 264. https://doi.org/10.3390/aerospace9050264

[43] H.C. Garner, E.W. Rogers, W.E. Acum, E.C. Maskell, Subsonic Wind Tunnel Wall Corrections, NATO-AGARD, 1966.